

**Climate Change of the twentieth through twenty-first centuries simulated by the
MRI-CGCM2.3**

Seiji Yukimoto, Akira Noda, Takao Uchiyama, and Shoji Kusunoki

Meteorological Research Institute, Tsukuba, Japan

Submitted to Papers in Meteorology and Geophysics

28 April, 2005

Abstract

Experiments for the twentieth century historical climate change and the twenty-first century scenario are performed with the latest version of the MRI climate model MRI-CGCM2.3. The model reproduced the globally averaged surface air temperature (SAT) variation in the twentieth century with a good agreement in the interdecadal change of the observed trend, as well as the overall SAT increase of 0.5°C relative to the pre-industrial level. In the scenario experiment for the IPCC SRES-A1B, the globally averaged SAT rise 2.4°C in the late twenty-first century. Spatial structures of the simulated trends for the late twentieth century are validated in various atmospheric fields by comparing with observed data, and proved that the model demonstrates reasonable agreement in each fields with the observed trend. Most of the simulated changes for the twenty-first century are projected onto those trends appeared in the late twentieth century. The simulated patterns of the sea level pressure (SLP) in the both hemispheres bear a resemblance to the observed trends, with each spatial structure is reminiscent of the Northern Hemisphere and the Southern Hemisphere annular modes (NAM and SAM, respectively). These SLP trend patterns are consistent with the trends in the SAT, precipitation and zonal mean zonal wind fields, similarly as in the NAM and SAM, and the coherent trend structures of these fields are projected to enhance in the twenty-first century climate change. The changes of ocean and sea ice with an association with these atmospheric changes are also described.

1. Introduction

Climate models have advanced and been sophisticated in recent years, and with such climate models, many simulations for projecting future climate change have performed. Based upon simulation results from such state-of-the-art climate models (e.g., Johns et al., 2001, Dai et al., 2001), assessments for the future climate change are made in the Third Assessment Report (TAR) of Inter-governmental Panel on Climate Change (IPCC, 2001). The Meteorological Research Institute (MRI) also contributed to the TAR with the results from a newly developed climate model MRI-CGCM2.0 (Yukimoto et al., 2001) at that time.

The MRI-CGCM2.0 has been updated and released as MRI-CGCM2.3 (Yukimoto et al., 2005), in which the performance in many aspects has improved. The model exhibits an excellent reproducibility in present-day climate, for example, meridional distributions of radiation budget and cloud radiative forcing close to the satellite observations (Yukimoto et al., 2005), and a seasonal migration of Asian monsoon (Rajendran et al., 2004), and so on. With using this model, we

performed experiments for reproducing historical climate and scenario experiments for future climate change. The results are opened to the public, for the use of detailed analyses by many researchers to make contributions to the 4th Assessment Report of IPCC (IPCC-AR4). Part of the experiment results are provided to the lower boundary data of the time-slice global warming experiments (Noda et al., 2005) with using a very high-resolution atmospheric climate model (Mizuta et al., 2005), in which changes of typhoons, mesoscale phenomena and extreme events with the global warming are studied. In the present paper, we describe results of preliminary analysis about the climate changes as a fundamental information for these studies.

Evaluating reproducibility with a climate change simulation for the twentieth century is one of the useful measures assessing a reliability of climate models used for future climate change prediction. There are many kinds of known historical external forcing affecting on the climate system, such as variations of anthropogenic greenhouse gases and sulfate aerosols, in addition to natural source forcings from the solar activity and volcano eruptions that load radiative forcing by their stratospheric aerosols. In historical climate simulations, these known natural and anthropogenic external forcing agents are imposed to a climate model, and the simulated climate change in the twentieth century is compared with the observations.

The instrumental observation that covers global domain and long temporal period sufficient to detect climate changes in response to such forcings. In the Northern Hemisphere (NH), however, observations of the surface air temperature (e.g., Jones et al., 1999) and the sea level pressure (e.g., Trenberth and Paolino, 1980) have relatively large coverage in the past centuries. These observations can be used for examining how the climate model reproduces the historical climate changes.

We validate the results in the last 30 years of the twentieth century that has relatively high observation densities, and examine how the climate trends in the twentieth century captures potential climate changes in the twenty-first century.

The Arctic Oscillation (AO) and the Antarctic Oscillation (AAO), also referred to as the Northern Annular Mode (NAM) and the Southern Annular Mode (SAM), respectively, are known as the most dominant variability in the atmosphere (Thompson and Wallace, 2000, Limpasuvan and Hartmann, 1999), that accompany a mass displacement between polar cap region and surrounding midlatitudes. In the past few decades, indices of these modes exhibit remarkable increase trend (deepening of the polar low pressure) (e.g., Thompson et al., 2000, Marshall, 2003), which may be related to human influences such as increase of greenhouse gas concentrations, and exerted a great influence on the climate change in the twentieth century. Thompson et al. (2001) suggested that a large part of the climate trends in the last 30 years of the twentieth century can be accounted by components

congruent to the AO trend.

It is a matter of concern to study whether these observed changes in the atmospheric general circulation caused by external forcing or internal variability, or how the modes will change in the future climate. Some of the models simulated the changes toward positive phase of the AO (e.g., Shindell et al., 1999, Fyfe et al., 1999) and AAO (e.g., Cai et al., 2003) in an experiment with doubled carbon dioxide concentration or a scenario experiment, though until now there is no consensus about the historical nor future change. From the results of historical experiments with the MRI-CGCM2.3, it is shown that response to external forcing exhibits an interdecadal variation that has a sea level pressure pattern similar to the AO (Yukimoto and Kodera, 2005). Involving analyses for overall climate change, we demonstrate how this variation influence on the changes in the surface temperature and other climate fields, and how it will evolve in the twenty-first century in the scenario experiments.

This paper is constructed as follows; Section 2 gives a brief description of the model, and Section 3 describes the experimental design. Section 4 demonstrates the results of the historical experiments and the scenario experiments. Summary and discussion are given in Section 5.

2. Model

The model used for the present study is the latest version of the MRI climate model referred to as MRI-CGCM2.3. The model is improved chiefly with its cloud scheme and some other physical parameterizations from the early version of the model (MRI-CGCM2.0, Yukimoto et al., 2001), but retaining the fundamental framework. Detailed description of the model and model's performance in the control climate are given in Yukimoto et al. (2005).

The atmospheric component has horizontal T42 resolution (approximately 280 km transform grid) and 30 layers in vertical with the top at 0.4 hPa. Longwave radiation is calculated by a multi-parameter random model formulated by Shibata and Aoki (1989), which explicitly addresses absorption by methane (CH₄) and nitrous oxide (N₂O) in addition to water vapor (H₂O), carbon dioxide (CO₂), and ozone (O₃). For solar radiation calculation, a delta-two-stream approximation method by Shibata and Uchiyama (1992) is used. Scattering of solar radiation by atmospheric aerosols (direct effect) is explicitly treated. Penetrative convection is parameterized with using an Arakawa-Schubert scheme based on a prognostic mass flux formulated by Randall and Pan (1993). The model treats clouds with a diagnostic cloud scheme based on functions of relative humidity. By improving the vertical profile of the critical relative humidity to form a cloud, the model simulates the distribution of radiation budgets close to the observation, resulting a good performance, for

instance, in the implied ocean meridional heat transport and distributions of the precipitation.

The model exhibits a larger and approximately doubled climate sensitivity (2.6K) compared to the former version. This is mainly attributable to the response of low clouds to the surface warming with the CO₂ increase (Yukimot et al., 2005).

The oceanic component is a Bryan-Cox-type global ocean general circulation model (OGCM). The horizontal resolution is 2.5 degrees in longitude and 2.0 degrees in latitude at poleward of 12°S and 12°N with finer resolution up to 0.5 degrees near the equator. The vertical 23 levels are unevenly placed between the surface and the deepest bottom at 5000m that forms a realistic topography. The sea ice model calculates compactness and thickness prognostically based on thermodynamics and horizontal advection and diffusion. The advection velocities are determined from the surface ocean current multiplied by an empirical constant (set to one-third at present).

We employ flux corrections for the experiments. With the improvements in the latest version, the model is now able to reproduce reasonably realistic climate without employing flux corrections. However, we believe it is more important to simulate climate change on the basic state that is close to the reality as much as possible, since the results will be provided for studies of regional scale.

3. Experiments

Experiments analyzed in the present paper includes a ‘pre-industrial’ control experiment (PIctrl), a historical climate experiment for the twentieth century (20C3M), and three SRES (IPCC, 2000) scenario experiments for the twenty-first century. The abbreviations follows the convention for the IPCC AR4. The forcing agents of the experiments and the configurations of individual experiments (summarized in Table 1) are described.

a. Forcing agents

External forcing for the present experiments consists of four category of agents, namely, greenhouse gas concentrations, tropospheric sulfate aerosol, solar irradiance, and shortwave radiative forcing due to volcanic stratospheric aerosols.

The greenhouse gases imposed by specifying as well-mixed concentrations include three species, namely, CO₂, CH₄, and N₂O. Forcing due to chlorofluorocarbons (CFCs), which are not explicitly treated in the model’s radiation scheme, is imposed as additional CO₂ concentration with equivalent radiative forcing. Note that ozone concentration change is not included in the forcing for the present experiments.

The tropospheric sulfate aerosol forcing is imposed only for direct effect (scattering of solar radiation by aerosol droplets). The aerosol includes both natural and anthropogenic sources.

Column total sulfate aerosol from natural source is estimated as a residual from the total and anthropogenic sulfate mass distributions (the data available at <http://gacp.giss.nasa.gov/transport/>) derived by the GACP transport model by Tegen et al. (1997). Distribution of the natural source sulfate aerosol shows a larger amount over the tropical ocean because of the marine biogenic dimethylsulfide (DMS) emission.

The solar activity forcing is simply imposed by changing the solar constant, and the spectral change associated with the solar activity is not included. The reconstructed historical record of the total solar irradiance is based on Lean et al. (1995) and are available at <http://www.giss.nasa.gov/data/simodel/solar.irradiance/>. The reconstruction data includes 11-year activity cycle and a longer-term component based on the sunspot variations.

The effect of stratospheric aerosols due to the volcanic activity is introduced by reducing the solar irradiance at the model's top of atmosphere (by changing the solar constant) as a substitution. A "direct" response of the lower stratosphere to volcanic forcing differs from solar forcing that is equivalent for the troposphere and ocean (e.g., Shindell et al., 2001). However, volcanic forcing has a relatively short time scale (at most a couple of years), so we believe the substitution does not greatly affect the present results focusing on the long-term climate change. The magnitude of the reduction is linearly scaled so that the global averaged radiative forcing fits to the estimation by Sato et al. (1993). The data is obtained from <http://www.giss.nasa.gov/data/strataer/>.

b. Preindustrial control experiment (PIcntrl)

The PIcntrl simulates an unperturbed climate state with anthropogenic forcings at the pre-industrial level, and is used as the reference for the following historical and scenario experiments. Also the PIcntrl provides initial states for the 20C3M simulations.

The initial state of the simulation is taken from the final state of the 450-year pre-industrial spin-up (PIspup) integration which initiated from the end of the present-day spin-up integration (428 year length, See Yukimoto et al., 2005). The PIspup is integrated with a fully coupled mode, and is long enough so that there is little climatic drift at least in the upper ocean. The length of the PIcntrl simulation is 350 years.

The forcing agents for the PIspup and PIcntrl simulations are fixed at levels of year 1850, i.e., $\text{CO}_2 = 290$ ppmv, $\text{CH}_4 = 792$ ppbv, $\text{N}_2\text{O} = 285$ ppbv, CFCs = 0, solar constant = 1366.0 Wm^{-2} , and the sulfate aerosol from natural source only. The aerosol mass is given in the column total and is vertically distributed with a homogeneous mixing ratio in the lowest 740 m thickness of the atmosphere. The volcanic forcing is not included.

c. Historical experiment (20C3M)

The 20C3M is an experiment for simulating the climate change of the twentieth century, by imposing known historical records of external forcing. The results of the 20C3M are evaluated for assessing how the model can reproduce the past climate change, and also provide initial states for the SRES scenario experiments.

The 20C3M experiment consists of five member ensemble simulations. By taking the ensemble average, dependency on initial conditions and the internal variability can be eliminated. The initial state of each member simulation is taken from the different states of the PIcntrl simulation at 1, 51, 101, 151, and 200th year. The period of each simulation is 150 years from 1850 through 2000.

The forcing agents of the experiment are the historical record of (or estimated) greenhouse gases (CO₂, CH₄, N₂O and CFCs), tropospheric sulfate aerosol, volcanoes and solar forcing. Temporal change of each greenhouse gas concentration is specified by the data after Hansen et al. (1998), which are available from <http://www.giss.nasa.gov/data/simodel/ghgases/>. The total mixing ratio of CFCs are converted to equivalent CO₂ and added to the CO₂ concentration. The radiative forcing by the total halocarbons is scaled as 0.3 Wm⁻² at the level in 1990 and is included as 21 ppmv of equivalent CO₂.

The column total tropospheric sulfate mass loading with a geographical distribution is specified and vertically distributed with a homogeneous mixing ratio in the lowest 740 m thickness of the atmosphere. The temporal variation is included with multiplying a weighting time-series based on the historical emission record. The sulfate mass loading data is from Mitchell and Johns (1997).

The historical forcing variations of solar and volcanic activity is imposed as the solar constant variation as mentioned above.

d. Scenario experiments (SRES)

The SRES scenario experiments simulate the climate change in the twenty-first century imposing future anthropogenic forcings based on SRES marker scenario (IPCC, 2000). In the present study, A1B, A2 and B1 scenarios (abbreviated experiment names are SRESA1B, SRESA2, AND SRESB1, respectively) are used. Each experiment consists of five member ensemble simulations. Each member simulation starts from the state of respective year 1990 in the 20C3M simulations, although the 20C3M simulations are extended until year 2000. The period of the simulations covers from 1990 through 2100 (111 year length).

Temporal changes of concentration for CO₂, CH₄, and N₂O are specified for each marker scenario. The concentration data are provided by IPCC (2001, Appendix II.2) which are based on the ISAM-model. The concentration change of CFCs is not included. Three-dimensional distributions of sulfate aerosol for the SRES experiments are derived by the MRI chemical transport model (MASINGAR, Tanaka et al., 2003) for every 10 years in each scenario. Temporal change of

global total sulfate mass loading (unit: Tg) for each SRES marker scenario is shown in Fig. 1. There are no variations of the solar activity and volcanic activity in the SRES experiment, so the solar constant is fixed at 1367 Wm^{-2} .

4. Results

a. Radiative forcing

Temporal variations of the global averaged net radiative forcing at the tropopause for the 20C3M and SRES experiments are illustrated in Fig. 2. These are results of all the external forcing imposed for each experiment. At the end of the twentieth century, the radiative forcing increased approximately 1.5 Wm^{-2} relative to the pre-industrial level. The increase rate is larger in the last 30 years of the twentieth century than in the preceding period, owing to a rapid increase of anthropogenic greenhouse gases. There are number of pulses with negative forcing due to major volcanic eruptions with the maximum magnitude of 1 Wm^{-2} . There is an active period in the late nineteenth century, revealed as a depression of the radiative forcing, followed by a relatively calm period until 1963 eruption of Agung (Indonesia), and outstanding pulses due to the eruptions of El Chichon (Mexico) in 1982 and Pinatubo (Philippine) in 1991.

For scenario experiments, the SRESA2 exhibits the largest increase of the forcing exceeding 4 Wm^{-2} at the late twenty-first century, and A1B exhibits more rapid increase than A2 in the former half of the century but a modest increase afterwards and receives 3.4 Wm^{-2} at the end of the century. The forcing in the SRESB1 shows the least increase and almost no increase at the late twenty-first century with getting 2.2 Wm^{-2} .

b. Surface air temperature

The globally averaged annual mean surface air temperature (SAT) simulated in each experiment is shown in Fig. 3, together with that from the observation (HadCRU, Parker et al., 2004). The ensemble means and ensemble scatters are displayed. The values are plotted as deviations from the reference climate of 1961-1990 average.

Relative to the pre-industrial level, increase of the simulated SAT in 1961-1990 average is $0.5 \text{ }^\circ\text{C}$, This value agrees with the observed SAT change for the same period.

The rate of increase in 1970s through 2000 shows a good agreement with that observed which lies within the simulated ensemble scatter. Detailed fluctuation also appears to agree for the instantaneous dents related to the outstanding volcanic events in 1982 and 1991, showing coincidence between ensembles and the observation.

The observed warming around 1940 is underestimated in the simulation, and the observed

negative trend in 1940s through 1960s is not clear. In 1880s, the model simulates the SAT lower than observed, though the observation is very limited in the nineteenth century. In order to compare the anomalies between the simulated and observed global average, the same grid masking of missing data in the observation is applied.

In the scenario experiments, the rate of SAT increase in the early twenty-first century is close to each other, but reveals differences in the middle through late the century corresponding to the different forcing scenarios. The SRESA2 shows the largest warming in the late twenty-first century with over 3 °C increase at the end of century, and suppressed increase in the latter half for the SRESA1B leads to about 0.5 °C lower increase. The SRESB1 experiment exhibits the lowest increase throughout the twenty-first century.

The SAT changes are averaged for the target 20-year period of 2080-2099 and shown in Table 2. The target period is selected because the same period is used for providing the boundary data in the time-slice experiments by Noda et al. (2005). The averages of temperature increase for SRESA1B, SRESA2, and SRESB1 are 2.4, 2.7 and 1.7 °C, respectively.

Linear trends of the SAT change are estimated for each experiments and the observation, for selected 30-year periods in interest, and depicted in Fig. 4. The observed trends show an increase trend of 0.13 (± 0.04) K/decade in 1911-1940, a weak decrease trend of -0.03 (± 0.05) K/decade in 1941-1970, and a large increase trend of 0.19 (± 0.05) K/decade in the last 30 years of the twentieth century. The simulated trends in the 20C3M show notable agreement with this observed interdecadal change of the trends. Magnitude of the positive trend of 0.17 (± 0.04) K/decade in 1971-2000 is close to the observed value, though the increase trend in 1911-1940 is underestimated, and no negative trend is seen in 1941-1970 (though it is within the error bar for the observation).

The SRESA1B shows change of the trends from 0.28 (± 0.02) K/decade in 2041-2070 to 0.16 (± 0.02) K/decade in the last 30 years of the twenty-first century, whereas the SRESA2 shows large (0.35-0.36 K/decade) positive trends with similar magnitudes throughout the century.

Geographical distribution of the annual-mean SAT trends are examined for 30-year periods of 1971-2000 for the late twentieth century trends and 2071-2100 for the late twenty-first century trends, as shown in Fig. 5.

The observed late twentieth century trend indicates large increase trends over the continents in the middle-eastern Eurasia and the northern North America. Basin scale pattern is seen in the Pacific, with a suppressed warming or a slight cooling in the mid-latitude North Pacific, and a relatively large warming in the central-eastern tropical Pacific, which resembles the dominant interdecadal variability in the Pacific known as the Pacific decadal oscillation (PDO, Mantua, 1997).

The 20C3M ensemble (Fig. 5b) also exhibits a large warming trend over the Eurasia continent, though it is shifted north-westward than in the observation, and the trend over the North America is small. There are large increase trends in the marginal sea ice region in the Arctic Ocean, which are associated with decreases of sea ice coverage and thickness as shown in later. However, these warming is not seen in the observed trend. Since the observation dataset uses sea surface temperature (SST) over the ocean instead of SAT, and air temperature over sea ice region is largely apart from the SST in winter, it is not appropriate for comparison with the simulated SAT over the sea ice region. A weak cooling trend is simulated in the Labrador Sea and the south edge of Greenland. Although the cooling trend is not obvious in the observation for the annual mean trend, however, the observed trend for winter (not shown) exhibits a significant negative trend in that region.

The SRESA2 ensemble (that shows the largest global warming among the scenarios) reveals a similar large-scale geographical pattern to the 20C3M but with globally larger positive values, and the warming trends are very intense in the marginal sea ice region in the Arctic Ocean. The ‘El Niño-like’ pattern in the tropical Pacific is prominent, though it is not apparent in the 20C3M ensemble. The relatively larger warming trends over land in the Sahara through Middle East, South Africa, and Australia become significant, which also share regionality with the observed twentieth century trends.

To assess similarities of the geographical pattern of the SAT trends, spatial correlations are calculated for the late twentieth century (1971-2000) trends for the observation and 20C3M and the mid-twenty-first century trend (2041-2070) for the SRES experiments with each other (Table 3). In the calculation, a weighting by square of cosine of the latitude is used.

The simulated twentieth century trend in the 20C3M ensemble has low (0.14) spatial correlation with the observed trend. However, one of the ensemble members (run-4, Fig. 5c) has sizable similarity (0.28) with the observation. Broad geographical pattern agrees well, though the correlation is not so high due to their small structured differences. A PDO-like pattern in the Pacific shows a striking agreement with a negative trend in the central-eastern North Pacific and a positive trend in its southeastern side extending to the eastern tropical Pacific. This implies that a sizable part of the observed twentieth century trend contains internal variability such as PDO, particularly over the ocean.

The simulated trend patterns exhibit relatively higher spatial correlations among themselves. The 20C3M shows correlations over 0.6 with SRESA1B and SRESA2, suggesting an evidence that a large part of the ensemble twentieth century trend is a manifestation of the response to anthropogenic forcing. It seems that the SRESB1 shows a somewhat different response. This may

be related to its overall small climate change trend, leading to a relatively larger internal (natural) variability.

Seasonal differences of the SAT change in the SRES experiments are examined for 20 year averages for 2080-2099. Figure 6 shows the geographical distribution of the SAT changes for December to January (DJF) mean and June to August (JJA) mean.

In the low latitudes, both seasons reveal similar feature to each other and also to the annual-mean trend pattern. In the high latitudes, on the other hand, the warming is large in winter and small in summer. Particularly, in the marginal sea ice regions where the sea ice significantly decreases (Spitsbergen through Novaya zemlya and the Chukchi Sea in the Arctic Ocean, Sea of Okhotsk, and the Antarctic Ocean), the model simulates very strong warming in winter.

The geographical patterns of the averaged SAT change in the SRES experiments have little difference among themselves (the spatial correlations are over 0.98 with each other), and they are also similar with the result from a transient climate response (TCR) experiment reported by Yukimoto et al. (2005). Besides for the SAT, spatial structure differences in the changes are also small for other variables, therefore hereafter, we will basically demonstrate changes only for results from the SRESA1B.

Spatial correlations between the simulated late twentieth century trends and the simulated seasonal (DJF and JJA) changes (averages for 2080-2099) for the each SRES experiments are examined (Table 4). The spatial patterns of the SAT change exhibit correlations of 0.55 to 0.67 with the late twentieth century trends, with higher correlations in winter for all the scenarios.

c. Precipitation

Corresponding to the simulated global warming, the globally averaged precipitation consistently increases. The changes averaged for 2080-2099 indicate increases of 5.4%, 5.7% and 3.7% for the SRES A1B, A2 and B1 ensembles, respectively, relative to the 1961-1990 average in the 20C3M ensemble (Table 2).

Figure 7 shows geographical distributions of precipitation change rate in the SRESA1B ensemble averaged for 2080-2099 relative to the 1961-1990 average in the 20C3M ensemble. The large-scale patterns for the precipitation change are also close to the results from the TCR experiment (Fig. 17 of Yukimoto et al., 2005) as well as for the SAT. For both seasons (DJF and JJA), precipitation increases in the high latitudes, but with a larger increase rate in winter. There are remarkable decreases around the Mediterranean and in the Central Asia, and a large percentage increase in the arid region of the southern part of Arabia through Pakistan. The notable increase in the central-eastern equatorial Pacific is associated with the El-Niño-like surface temperature change (Fig. 6).

Spatial correlations with the simulated twentieth century trends are also examined for the precipitation change rate (Table 4). The correlations are 0.22-0.31 in DJF and 0.44-0.50 in JJA. All the experiments indicate a higher geographical similarity in the northern summer (JJA) than in winter (DJF). Compared to the SAT changes, it is suggested that uncertainty would be larger in projecting a future precipitation change from the observed twentieth century trend because of a larger internal variance. However, the correlations among the SRES experiments (not shown) are very high (over 0.96), which implies there is a robust structure in the anthropogenic climate change signal.

d. Sea level pressure

The observed and simulated late twentieth century (1971-2000) trends of the Northern Hemisphere (NH) sea level pressure (SLP) are shown in Fig. 8. The SLP observation data used here is the HadSLP1 (an update of GMSLP2, Basnett and Parker, 1997).

The simulated trend for the 20C3M ensemble shows an annular pattern with a negative trend in the Arctic and a positive trend in the surrounding midlatitude band, and its broad feature resembles the AO pattern. Although the model can simulate realistic month-to-month AO (Yukimoto and Kodera, 2005), the pattern in the late twentieth century trend indicates several features different from such a short-term AO. One of the action center of the Atlantic sector in the AO pattern is not concentrated around Iceland, instead it is displaced toward the North Pole, and another action center over the Atlantic is shifted westward and extends to Mediterranean through central Asia. These features are consistent with the observed trend, though the observed trend shows somewhat different pattern in the North Pacific.

A hemispheric pattern of the NH winter SLP change in the SRESA1B ensemble (2080-2099 average, Fig. 9) is similar to the late twentieth century trends with a spatial correlation of 0.63, except that the positive anomaly in the Mediterranean shifted further westward and the negative anomaly in the Arctic becomes stronger around the Bering Strait.

Figure 10 shows the temporal variations of the NH winter (DJF) SLP regressed onto the simulated late twentieth century trend pattern (Fig. 8b), which demonstrate that how the trend pattern have been emerged and is detectable in the historical variation, and how it will evolve in the future climate. The temporal variations indicate a continuous increase from 1970s through the twenty-first century, suggesting that the annular trend pattern in the late twentieth century is embedded in the climate change signal in the twenty-first century. The regressions generally indicate increase tendency in the twenty-first century for all the SRES scenarios, though there are sizable interdecadal variations even with averaging five member ensembles, and differences among

the scenarios are not significant. These suggest that robustness of the climate change signal is modest in the NH SLP, since there is a large internal variability.

In the Southern Hemisphere (SH), the SLP trend reveals an annular pattern that is similar to the observed SAM (Fig. 11). With examining each seasons (not shown) the pattern is dominant throughout a year, whereas the annular pattern trend in the NH is dominant only in winter. This is possibly related to the climatological characteristics in the SH with much longer lasting polar vortex and the SAM is observed all seasons (Hartmann, 1998).

The temporal variations regressed onto the trend pattern (Fig. 12) also indicate significant upward trend through twentieth century to twenty-first century for all the scenarios. The interdecadal variability appears smaller than in the NH, which enables us to recognize differences among the scenarios in the response to each forcing. It is interesting to note that the interdecadal trends, i.e., an increase trend from the early twentieth century until around 1940, a decrease trend in 1940s to 1960s, and a increase trend afterward, appear to coincide with the observed tendencies in the global averaged SAT (Fig. 3).

It is suggested that the observed trend of the SAM (e.g., Marshall, 2003; Renwick, 2004) is influenced by the ozone depletion in the lower stratosphere (Thompson et al., 2000). In the present experiments, however, the ozone change is not included in the forcing agents, which suggests that the annular pattern trend in the climate change can be emerged even without ozone change, though the response is expected to become stronger if the ozone depletion is accounted as a forcing.

e. Atmospheric zonal-mean fields

Meridional vertical structure of the simulated late twentieth century trends in the zonal-mean zonal wind for DJF mean is depicted in Fig. 13b. For a validation of the simulations, same calculation for the ECMWF reanalysis data (ERA-40, Simmons and Gibson, 2000) is also depicted (Fig. 13a).

The simulated trend reveals a westerly anomaly in the NH polar stratosphere extending down to the troposphere. This corresponds to an intensification of polar vortex, which shares a feature with the NAM. In the ERA-40, the trend indicates a weak westerly anomaly around 60°N in the troposphere and lower stratosphere, which partly agrees with the simulated trend but there is no signal of intensified vertical shear in the stratosphere. Statistical confidence level is low in the reanalysis stratospheric trend since there is a large interannual variance and the observation period is short, whereas the results from 20C3M experiment has higher confidence with a smaller internal variability by taking the ensemble average.

In the SH, the simulation exhibits a notable increase trend of westerly around 60°S that grows vertically from the surface to the stratosphere, accompanying a easterly trend at 40°S to consist a

meridional dipole structure. This feature is similar to the SAM and also well agree with the observed trend. This SAM-like trend is simulated remarkable in southern summer (DJF). Thompson et al. (2000) suggested that the positive trend of SAM is most marked in November, and they associated it with the ozone losses in spring. Our result does not contradict the seasonality of the observed trend, although our experiment does not include the ozone change. Also an easterly trend is simulated in the tropical upper troposphere, which seems consistent with the reanalysis data. Similarity of overall structure of the trend is evaluated by taking a spatial correlation (mass weighted), and the value for between the reanalysis and 20C3M is 0.52 (Table 4).

Trends in the zonal-mean air temperature (Fig. 14) are simulated with a typical structure, namely, a warming in the troposphere and a cooling in the stratosphere, which is a well-known response to increase of greenhouse gases, and is obviously different from that in the internal variability (Yukimoto and Kodera, 2005). This structure agrees with the observational trend in a broad-scale features. The simulated trend shows a strong cooling in the polar stratosphere in accordance with the intensification of polar vortex (Fig. 13b), though it does not appear in the reanalysis (which has below 95% statistical significance in that region). There is a strong cooling in the Arctic lower stratosphere (that has 95% significance), which can be associated with the effect of ozone depletion, since the model does not show such a signal.

For the late twenty-first century, the change of the zonal wind (Fig. 15a) is similar to that of the late twentieth century trend (Fig. 13b) in many aspects, and has a spatial correlation of 0.79 (Table 4). In the twenty-first century change, however, axis of the westerly anomaly in the winter NH inclines toward low latitude in the lower stratosphere. The change accompanies intensification and up and equator-ward shift of the subtropical jets in both hemispheres. This may be related to the uplift of the tropopause, but detailed analysis will be required for interpreting the change. The extratropical SH reveals the same structure as in the twentieth century trend.

The zonal-mean temperature structure (Fig. 15b) indicates good agreement (spatial correlation of 0.98, Table 4) with the simulated late twentieth century trend. There are significant warming about 4 K in the tropical upper troposphere and exceeding 6 K in the northern high latitude near the surface.

f. Ocean

Ocean temperature

The ocean temperature change in the SRESA1B experiments are examined for zonal average (Fig. 16). Except for the high latitudes, the ocean is evenly warmed by approximately 0.3 °C at 1000 m depth. A deep intrusion of the warming at 60°N is attributable to the deep overturning of

the Atlantic Ocean. In the interior Arctic Ocean, on the other hand, the warming is confined shallow due to a strong stability there.

Thermohaline circulation

The maximum Atlantic overturning (Fig. 17) indicates a decline with time, from 19 Sv in the early twentieth century to less than 18 Sv in the late twenty-first century in the SRESA1B and SRESA2 experiments. Different magnitude of weakening in the twenty-first century among the scenarios appears to roughly correspond to the magnitude of surface warming. Cause of these weakening can be explained by a strengthening of the upper ocean stability in the sinking region, as a result of freshening by the precipitation increase in the North Atlantic as seen in Fig. 7, in addition to the surface heating.

Sea level change

Sea level change is not climate change itself, but an important phenomenon that arises as a result of climate change and has a large social impact. The sea surface height changes owing to several factor, that is, thermal expansion of sea water, freshwater inflow from land water (melting of glaciers and ice sheets), and local height anomaly caused by ocean circulation change. Since the present model does not represent variations of glaciers nor ice sheets, only effects of the thermal expansion added to the local height anomaly change are examined.

In the late twenty-first century in the SRESA1B experiment, the globally averaged sea level rises 12.2 cm by the thermal expansion. Geographical distribution of the local height change (Fig. 18) indicates a relative higher anomaly in the North Pacific with a maximum of 20 cm in the east off Japan, and zonally elongated regions of high anomalies around 40°S in the Southern Ocean and relative lower anomalies around the Antarctica.

g. Sea ice

The sea ice significantly decrease both in its coverage and thickness according to the surface warming. Geographical distributions of the sea ice compactness change are depicted in Fig. 19. The sea ice retreats at marginal sea ice regions in both seasons of maximum and minimum extent. The retreat is more prominent in summer because of ice-albedo feedback, though its impact on the atmosphere is much smaller than in winter, since temperature difference between the sea ice surface and the sea ice free area is small in summer.

The total area and volume in the NH and SH for each experiments are shown in Table 5. In the NH, the maximum total sea ice area (March) decreases 14 % from $13.5 \times 10^{12} \text{ m}^2$ (20C3M: 1961-1990) to $11.6 \times 10^{12} \text{ m}^2$ (SRESA1B, 2080-2099), and the minimum area (September) decreases

37 % from $7.6 \times 10^{12} \text{ m}^2$ to $4.8 \times 10^{12} \text{ m}^2$. Reduction ratio of the winter area is small in the SH, and the total area in September decreases 7 % from $17.6 \times 10^{12} \text{ m}^2$ to $16.3 \times 10^{12} \text{ m}^2$, but in summer (March) the total area reduction is large (59 %).

The sea ice thickness markedly decreases according to the warming over the entire sea ice regions not only in the marginal regions (the distribution is not shown). In the NH, total volume of the sea ice decreases 45% from $38 \times 10^{12} \text{ m}^3$ to $17 \times 10^{12} \text{ m}^3$ in winter (March). In winter, the thickness reduction has a large impact on the surface temperature, because heat conduction in the sea ice becomes large, due to a large temperature gradient in the sea ice if the thickness become considerably thin.

5. Summary and Discussion

Experiments for the twentieth century historical climate change and the twenty-first century scenario are performed with the latest version of the MRI climate model MRI-CGCM2.3 that has been improved in the performance of reproducing the present-day climate (Yukimoto et al., 2005). In the historical experiment, ensemble simulations are performed with imposing the anthropogenic forcing from greenhouse gases of CO_2 , CH_4 , N_2O , and CFCs, and a direct effect of the tropospheric sulfate aerosol, and natural source forcing from the solar activity and a radiative effect of volcanic stratospheric aerosols, for the period from the mid-19C to the end of twentieth century. In the scenario experiments, the changes of greenhouse gas concentrations and tropospheric sulfate aerosol in the twenty-first century based on IPCC SRES are imposed.

The model reproduced the globally averaged SAT variation in the twentieth century with a good agreement in the interdecadal change of its trends. The simulated temperature rise at the late twentieth century (average of 1961-1990) relative to the pre-industrial level is $0.5 \text{ }^\circ\text{C}$ that agrees with the observed value. The simulated SAT trend in the last 30 years exhibits a quite good agreement with the observed trend, which suggests high reliability of the model in the projection of the future climate change. In the scenario experiments, the globally averaged SAT rise 2.4°C for SRESA1B, 2.7°C for SRESA2, and 1.7°C for SRESB1, in the late twenty-first century (average of 2080-2099).

The geographical distribution of the SAT change simulated for the twenty-first century reveals several reasonable features that have been shown in the many previous modeling studies. The geographical trend pattern of the NH winter SAT in the late twentieth century reveals a broad pattern similar to what is seen in the realistic model's AO (Yukimoto and Kodera, 2005). The trend pattern indicates a large warming trend in the region of the northern Eurasia extending to Japan and

a slight cooling around the Labrador Sea, which is expected to enhance in the twenty-first century with being overlaid on the globally averaged temperature rise. The experiments suggest a regional feature with a relative smaller warming around the Labrador Sea in the North Atlantic for the twenty-first century simulations, which is also reported in the previous studies. Cause of this feature has been explained as a result of the large ocean heat up-take associated with the deep overturning of the North Atlantic. The AO-like atmospheric circulation change probably contributes to the anomaly pattern in addition to that oceanic effect.

The simulated SLP trend pattern in the late twentieth century is also agree with the observed pattern. The NH winter SLP is simulated to decrease in the Arctic region and increase in the surrounding midlatitude band, representing an annular pattern sharing some features with the AO. Unlike the AO, however, the simulated pattern does not have the action center near Iceland, and center of the positive anomaly in the Atlantic shifts toward the Mediterranean. The SH SLP trend shows a year-round pattern close to the SAM pattern. The experiments suggest that the annular patterns in the both hemispheres appeared in the late twentieth century would growth along with the climate change during the twenty-first century, although the climate change signal in the NH is relatively smaller because of its larger internal variability.

The model reproduced an intensification of westerly wind in the extratropical troposphere, extending to the stratosphere with an equivalent barotropic vertical structure, in winter season for the NH and in almost year-round for the SH. The structures for both hemispheres are reminiscent of the NAM and SAM, respectively, and are projected onto the twenty-first century change. Up and equator-ward shift of the subtropical jets in the both hemispheres also simulated when the global warming become large in the twenty-first century, though it is not apparent in the twentieth century trend. The result is consistent with Kushner (2001) who reported with their climate model simulations that the SH extratropical response is strongly projected onto the model's SAM and also there are westerly wind anomaly in the tropical upper troposphere.

The experiments suggest that the zonally averaged temperature change is apparently dependent on the NAM and SAM, although the response of wind fields implied that the structure is projected onto those dominant variabilities. The structure includes familiar features in the previous studies (e.g., Mitchell et al., 1990; Rind et al., 1998), that is, a warming in the troposphere with a maximum in the tropical upper troposphere associated with the warmer moist adiabatic vertical profile and a cooling in the stratosphere associated with the enhanced radiative cooling by the increased greenhouse gases.

In the simulated twenty-first century climate, the precipitation increases both summer and winter seasons at high latitudes with a larger increase rate in winter. The AO-like atmospheric

circulation change is reflected on the remarkable precipitation increases in the northern Europe. Conjunction with the ocean surface warming, the increase of freshwater flux into the northern North Atlantic leads to stronger ocean vertical stability and possibly contributes to weaken the Atlantic overturning.

The sea level change in the twenty-first century is estimated by the effects from thermal expansion of seawater and ocean circulation change, and is projected to indicate a larger elevation in the midlatitude northwestern Pacific with a maximum in the east off of Japan. This regional sea level change is attributable to a northward shift and enhancement of the North Pacific subtropical gyre. The Sverdrup streamfunction anomaly (not shown) calculated from the ocean surface wind stress change suggests a good agreement with the sea level change anomaly, which implies that the high pressure anomaly over the North Pacific simulated with the climate change (Fig. 9) contributed to this.

From many aspects, we evaluated the historical climate changes simulated by the model, and found that the model demonstrated the changes consistent with the observed trends in the twentieth century. These results support the reliability of the model in the projection of the twenty-first century climate change. More detailed analyses using the results of these model experiments are expected to achieve a lot of understanding.

Acknowledgements.

The authors are grateful to K. Kodera and Y. Kuroda for valuable comments and discussion. This work was funded by the Climate Change Prediction Fund (Study of the Prediction of Regional Climate Changes over Japan due to Global Warming) under Japan Meteorological Agency. A part of the computation is performed on the supercomputer at the Center for Global Environmental Research, the National Institute for Environmental Studies.

References

- Basnett, T. and D. Parker, 1997: Development of the Global Mean Sea Level Pressure Data Set GMSLP2, Climate Research Technical Note, 79, Hadley Centre, Met Office, FitzRoy Rd, Exeter, Devon, EX1 3PB, UK.
- Cai, W.J., P.H. Whetton, and D.J. Karoly, 2003: The response of the Antarctic Oscillation to increasing and stabilized atmospheric CO₂. *J. Climate*, **16**, 1525-1538.
- Dai, A., T.M.L. Wigley, A. Boville, J.T. Kiehl, and L.E. Buja, 2001: Climates of the twentieth and twenty-first centuries simulated by the NCAR Climate System Model. *J. Climate*, **14**, 485-519.
- Fyfe, J.C., G.J. Boer, and G.M. Flato (1999), The Arctic and Antarctic Oscillations and their projected changes under global warming. *Geophys. Res. Lett.*, **26** 1601-1604.
- Dennis L. Hartmann and F. Lo, 1998: Wave-driven zonal flow vacillation in the Southern Hemisphere. *J. Atmos. Sci.*, **55**, 1303-1315.
- Hansen, J., M. Sato, A. Lacis, R. Ruedy, I. Tegen, and E. Mathews, 1998: Climate forcings in the industrial era. *Proc.*

Natl. Acad. Sci. USA, **95**, 12753-12758.

IPCC, 2000: Special Report of the Intergovernmental Panel on Climate Change. Nebojsa Nakicenovic and Rob Swart (Eds.), Cambridge University Press, UK. pp 570.

IPCC, 2001: Climate Change 2001: The Scientific Basis, Intergovernmental Panel on Climate Change, Contribution of Working Group I to the Third Assessment Report of the Intergovernmental Panel on Climate Change. (Eds. Houghton, J.T., Y. Ding, D.J. Griggs, M. Noguer, P.J. van der Linden, X. Dai, K. Maskell, and C.A. Johnson), Cambridge University Press, Cambridge, United Kingdom and New York, NY, USA, 881pp.

Johns, T.C., J.M. Gregory, W.J. Ingram, C.E. Johnson, A. Jones, J.A. Lowe, J.F.B. Mitchell, D.L. Roberts, D.M.H. Sexton, D.S. Stevenson, S.F.B. Tett and M.J. Woodage, 2001: Anthropogenic climate change for 1860 to 2100 simulated with the HadCM3 model under updated emissions scenarios. Hadley Centre Technical Note No. 22, available from The Hadley Centre for Climate Prediction and Research, The Met Office, London Road, Bracknell, RG12 2SY, UK.

Jones, P.D., M. New, D.E., Parker, S. Martin, and I.G., Rigor, 1999: Surface air temperature and its variations over the last 150 years. *Reviews of Geophysics* **37**, 173-199.

Kushner, P.J., I.M. Held, and T.L. Delworth, 2001: Southern Hemisphere atmospheric circulation response to global warming. *J. Climate*, **14**, 2238-2249.

Lean J., J. Beer, and R. Bradley, 1995: Reconstruction of solar irradiance since 1610; implications for climate change, *Geophys. Res. Lett.*, **22**, 3195-3198.

Limpasuvan, V., and D. Hartmann, 1999: Eddies and the annular modes of climate variability. *Geophys. Res. Lett.*, **26**, 3133-3136.

Mantua, N.J. and S.R. Hare, Y. Zhang, J.M. Wallace, and R.C. Francis, 1997: A Pacific interdecadal climate oscillation with impacts on salmon production. *Bull. Amer. Meteor. Soc.*, **78**, 1069-1079.

Marshall, G.J., 2003: Trends in the Southern Annular Mode from Observational and Reanalyses. *J. Climate*, **16**, 4134.

Mitchell, J.F.B., T.C. Johns, 1997: On modification of global warming by sulfate aerosols. *J. Climate*, **10**, 245-267.

Mitchell, J., S. Manabe, V. Meleshko, and T. Tokioka, 1990: Equilibrium climate change and its implications for the future. Climate Change. The IPCC Scientific Assessment. G. J. J. T. Houghton and J. Ephraums, Eds., Cambridge University Press.

Mizuta, R., K. Oouchi, H. Yoshimura, A. Noda, K. Katayama, S. Yukimoto, M. Hosaka, S. Kusunoki, H. Kawai, and M. Nakagawa, 2005: 20km-mesh global climate simulations using JMA-GSM model. (*submitted to J. Meteor. Soc. Japan*)

Noda, A., S. Kusunoki, J. Yoshimura, H. Yoshimura, K. Oouchi, and R. Mizuta, 2005: Global warming projection by an atmospheric general circulation model with 20-km grid size. (*Submitted to Nature*)

Parker, D.E., Alexander, L.V. and Kennedy, J., 2004: Global and regional climate in 2003. *Weather*, **59**, 145-152.

Rajendran, K., A. Kitoh, and S. Yukimoto, 2004: South and East Asian monsoon climate and variation in the MRI coupled model (MRI-CGCM2). *J. Climate*, **17**, 763-782.

Renwick, J.A., 2004: Trends in the Southern Hemisphere polar vortex in NCEP and ECMWF reanalyses. *Geophys. Res.*

Letts., **31**, doi:10.1029/2003GL019302.

Rind, D., D. Shindell, P. Lonergan, and N. K. Balachandran, 1998: Climate change and the middle atmosphere. Part III: The doubled CO₂ climate revisited, *J. Climate*, **11**, 876-894.

Sato, M., J.E. Hansen, M.P. McCormick, and J.B. Pollack, 1993: Stratospheric aerosol optical depth, 1850-1990, *J. Geophys. Res.*, **98**, 22987-22994.

Shindell D., G.A. Schmidt, R.L. Miller, D. Rind, 2001: Northern Hemisphere winter climate response to greenhouse gas, ozone, solar, and volcanic forcing. *J. Geophys. Res., D, Atmos.*, **106**, 7193-7210.

Simmons, A. J., and J. K. Gibson, 2000: The ERA-40 Project plan, ERA-40 Proj. Rep. Ser. 1, 63 pp., Eur. Cent. for Medium-Range Weather Forecasts, Reading, UK.

Tanaka, T., K. Orito, T. Sekiyama, K. Shibata, M. Chiba and H. Tanaka, 2003: MASINGAR, a global tropospheric aerosol chemical transport model coupled with MRI/JMA98 GCM: Model description, *Pap. Meteor. Geophys.*, **53**, 119-138.

Tegen, I., P. Hollrig, M. Chin, I. Fung, D. Jacob, and J. Penner 1997: Contribution of different aerosol species to the global aerosol extinction optical thickness: Estimates from model results. *J. Geophys. Res.* **102**, 23895-23915.

Trenberth, K.E., D.A. Paolino Jr., 1980: The Northern Hemisphere sea-level pressure data set: trends, errors and discontinuities. *Mon. Wea. Rev.*, **108**, 855-872.

Yukimoto, S. and K. Kodera, 2005: Interdecadal Arctic Oscillation in twentieth century climate simulations viewed as internal variability and response to external forcing, *Geophys. Res. Lett.*, **32**, L03707.

Yukimoto, S., A. Noda, A. Kitoh, M. Hosaka, H. Yoshimura, T. Uchiyama, K. Shibata, O. Arakawa, and S. Kusunoki, 2005: The Meteorological Research Institute Coupled GCM, Version 2.3 (MRI-CGCM2.3), -- Control climate and climate sensitivity --. *Submitted to J. Meteor. Soc. Japan*.

Figure captions

Fig. 1 Temporal change of global total sulfate mass loading (unit: Tg) imposed for SRESA1B (thick solid), SRESA2 (dashed line) and SRESB1 (thin solid) experiments.

Fig. 2 Temporal variations of the global averaged net (longwave + shortwave) radiative forcing at the tropopause for the 20C3M (thin solid) and SRES (A1B: thick solid, A2: dashed, and B1: dotted lines) experiments.

Fig. 3 Temporal variations of the globally averaged annual mean SAT for the PIcntrl (grey), 20C3M (blue) and SRES (A1B: red, A2: orange, and B1: green) experiments and the observation (black). The ensemble means are plotted in lines and the ensemble scatters (ranges between the maximum and minimum) are plotted with shadings.

Fig. 4 Linear trends of the globally averaged annual mean SAT for the 20C3M (blue) and SRES (A1B: red, A2: orange, and B1: green) experiments and the observation (black) for the selected five 30-year periods (1911-1940, 1941-1970, 1971-2000 for historical periods and 2041-2070 and 2071-2100 for the future periods). Error bars denote 95% confidence limits estimated from interannual variance in each period.

Fig. 5 Geographical distributions of linear trends of the annual mean SAT for the (a) observation, (b) 20C3M (ensemble mean), and (c) 20C3M (run-4) for the period 1971-2000, and (d) SRESA2 for the period 2071-2100. The unit is K/decade.

Fig. 6 Geographical distributions of the simulated SAT change in SRESA1B ensemble averaged for 2080-2099 for (a) DJF mean and (b) JJA mean.

Fig. 7 Geographical distributions of the simulated precipitation change rate (%) in the SRESA1B ensemble averaged for 2080-2099 for (a) DJF mean and (b) JJA mean.

Fig. 8 Geographical distribution of linear trends of the DJF mean NH sea level pressure for the (a) observation (in hPa decade⁻¹) and (b) 20C3M ensemble (in hPa (30-yr)⁻¹), for the period 1971-2000.

Fig. 9 Geographical distribution of the NH (DJF mean) sea level pressure change in the SRESA1B ensemble (2080-2099 average, in hPa) relative to the 20C3M ensemble (1961-1990 average).

Fig. 10 Temporal variations of the NH (DJF mean) SLP change in the SRES ensembles (including the preceding 20C3M) regressed onto the 20C3M trend pattern for 1971-2000. A low pass filter with 20 year period is applied after the regression.

Fig. 11 Same as in Fig. 9, except for the SH annual mean SLP.

Fig. 12 Same as in Fig. 10, except for the SH annual mean SLP.

Fig. 13 Meridional vertical structure of the linear trends in zonal-mean zonal wind (DJF mean) for the (a) observation (ERA-40, unit is $\text{m s}^{-1} \text{decade}^{-1}$) and (b) 20C3M ensemble (unit is $\text{m s}^{-1} (30 \text{ yr})^{-1}$), for the period 1971-2000.

Fig. 14 Same as Fig. 13, except for zonal-mean air temperature (DJF-mean). Units are (a) K decade^{-1} and (b) $\text{K} (30 \text{ yr})^{-1}$.

Fig. 15 Meridional vertical structure of the zonal-mean changes in the SRESA1B ensemble (average for 2080-2099) relative to the 20C3M ensemble (average for 1961-1990) for the DJF-mean (a) zonal wind (ms^{-1}) and (b) air temperature (K).

Fig. 16 The zonally averaged annual-mean ocean potential temperature change (K) for the SRESA1B ensemble (average for 2080-2099) relative to the 20C3M ensemble (average for 1961-1990).

Fig. 17 Temporal variation of the maximum annual Atlantic overturning (Sv) with 5-year moving average for the 20C3M and SRES ensembles.

Fig. 18 The sea surface height change (cm) including global sea level change in the SRESA1B ensemble (average for 2080-2099) relative to the 20C3M ensemble (average for 1961-1990).

Fig. 19 The mean sea ice coverage change (fraction) in the SRESA1B ensemble (average for

2080-2099) relative to the reference climate (1961-1990 average in the 20C3M ensemble), for (a) NH in March, (b) NH in September, (c) SH in March, and (d) SH in September. The purple dashed lines denote regions of reference climate.

Tables

Table 1 Configurations of the experiments

Experiment name	period (year)	ensemble number	greenhouse gas concentrations				sulfate aerosol (direct effect)	solar forcing (solar constant, Wm^{-2})	volcano activity
			CO ₂ (ppmv)	CH ₄ (ppbv)	N ₂ O (ppbv)	CFCs (equiv. CO ₂)			
PIctrl	1851-2200	1	290	792	285	0	natural (GACP)	1366	0
20C3M	1851-2000	5	Hansen et al. (1998)				natural + anthrop. (GACP)	Lean et al. (1995)	Sato et al. (1993)
SRESA1B	1990-2100	5	IPCC (2001) SRES A1B			0	natural (GACP) + anthrop. (SRES A1B)	1367	0
SRESA2	1990-2100	5	IPCC (2001) SRES A2			0	natural (GACP) + anthrop. (SRES A2)	1367	0
SRESB1	1990-2100	5	IPCC (2001) SRES B1			0	natural (GACP) + anthrop. (SRES B1)	1367	0

Table 2. Temporal averages for surface air temperature and precipitation simulated in each experiments and changes from the reference climate (1961-1990 averages in the 20C3M).

Experiment	Average period (years)	SAT (Change) [°C]	Precipitation [mm/day] (Change)
20C3M	1961-1990	13.03	2.55
SRES-A1B	2080-2099	15.42 (2.39)	2.69 (5.4%)
SRES-A2	2080-2099	15.76 (2.73)	2.70 (5.7%)
SRES-B1	2080-2099	14.73 (1.70)	2.65 (3.7%)

Table 3 Spatial correlations among the SAT trend patterns for the observation (HadCRU), 20C3M, and SRES experiments.

	20C3M	SRESA1B	SRESA2	SRESB1
HadCRU	0.14	0.15	0.29	0.27
20C3M		0.69	0.64	0.34
SRESA1B			0.82	0.52
SRESA2				0.66

Table 4 Spatial correlations between the simulated late twentieth century trends (by 20C3M for 1971-2000), and the observed trends (1971-2000) and the simulated changes (SRES experiments, averages for 2080-2099) for the various fields.

	observations	SRES-A1B	SRES-A2	SRES-B1
SAT change (DJF)	0.10	0.67	0.67	0.64
SAT change (JJA)	0.10	0.60	0.55	0.61
precipitation change rate (DJF)	0.00	0.31	0.31	0.22
precipitation change rate (JJA)	-0.26	0.50	0.44	0.50
NH sea level pressure change (DJF)	0.57	0.63	0.50	-0.09
SH sea level pressure change (annual)	0.46	0.92	0.91	0.88
zonal mean zonal wind change (DJF)	0.52	0.79	0.83	0.81
zonal mean zonal wind change (JJA)	0.14	0.94	0.93	0.93
zonal mean air temperature change (DJF)	0.46	0.98	0.98	0.97
zonal mean air temperature change (JJA)	0.41	0.99	0.99	0.99

Table 5 Total area and volume in the NH and SH in March and September for each experiments

Experiment	Area [10^{12} m ²]				Volume [10^{12} m ³]			
	NH		SH		NH		SH	
	Mar.	Sep.	Mar.	Sep.	Mar.	Sep.	Mar.	Sep.
20C3M	13.5	7.6	3.5	17.6	38.1	29.2	1.9	11.8
SRESA1B	11.6	4.8	1.4	16.3	16.8	9.0	0.4	8.8
SRESA2	11.5	4.8	1.4	16.3	16.5	8.9	0.4	8.8
SRESB1	12.1	5.3	2.1	16.6	20.2	12.1	0.9	10.0

Figures

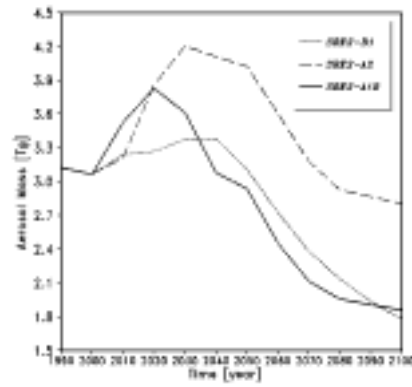


Fig. 1

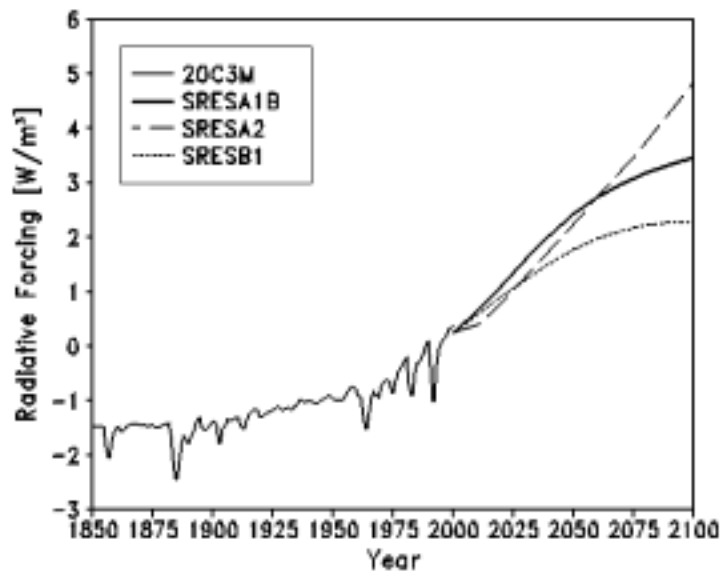


Fig. 2

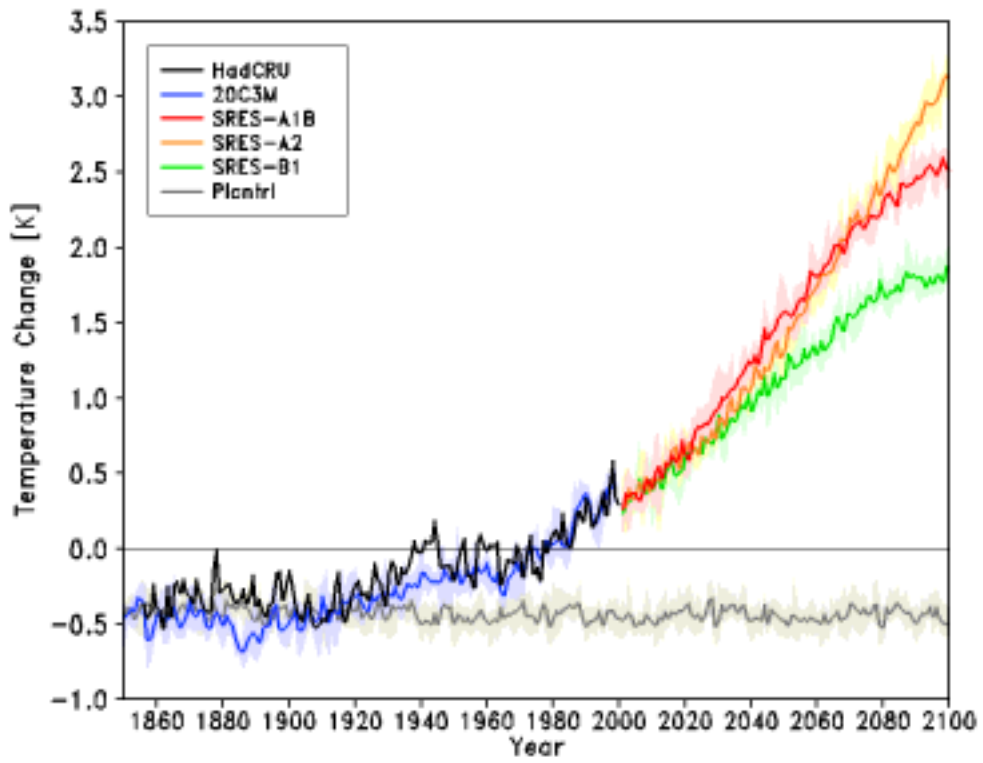


Fig. 3

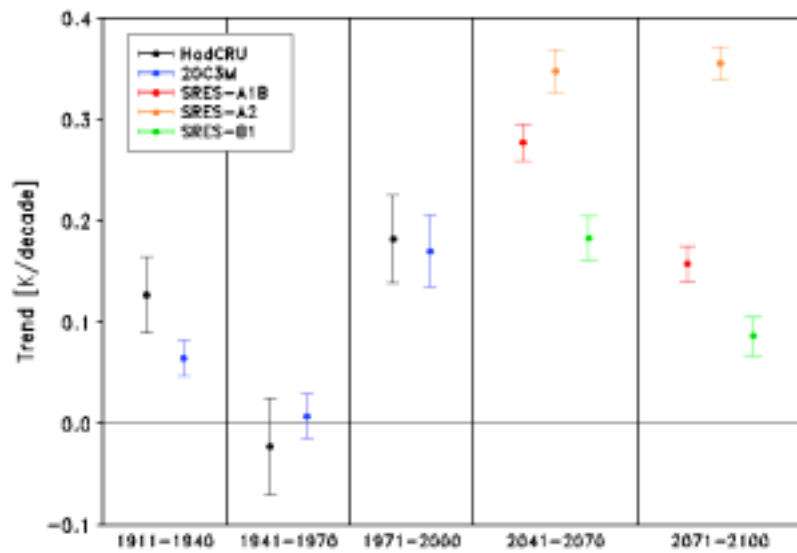


Fig. 4

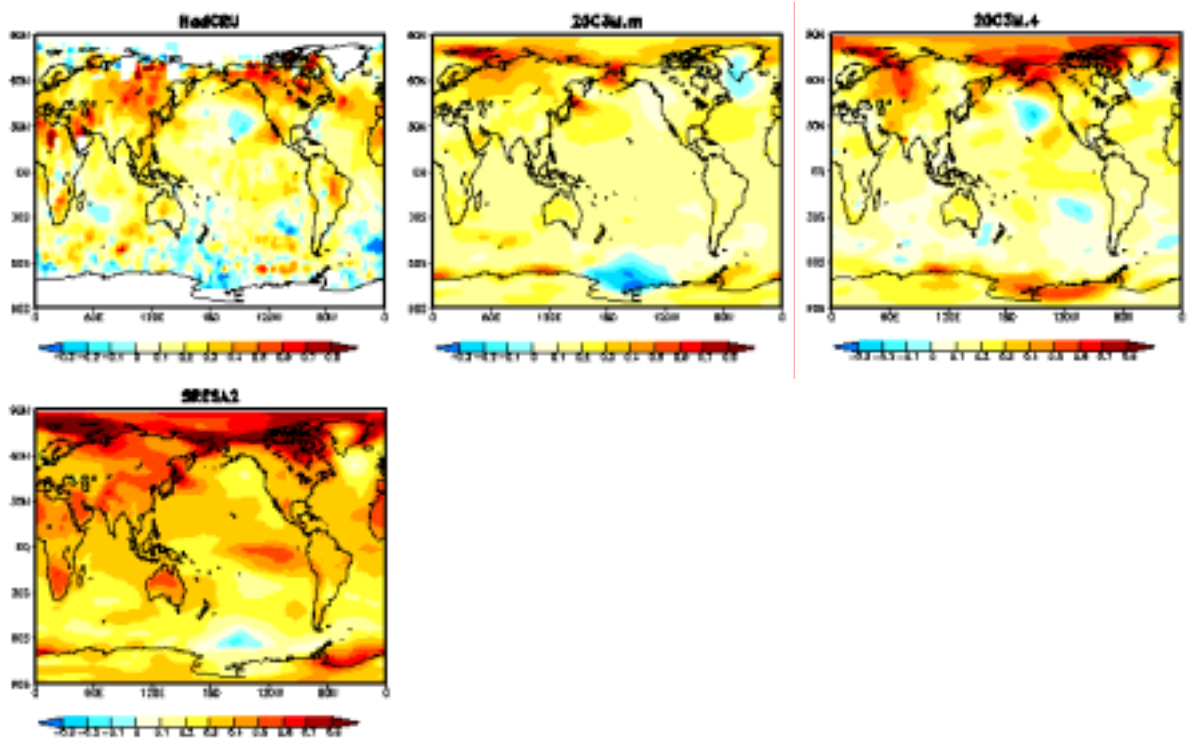


Fig. 5

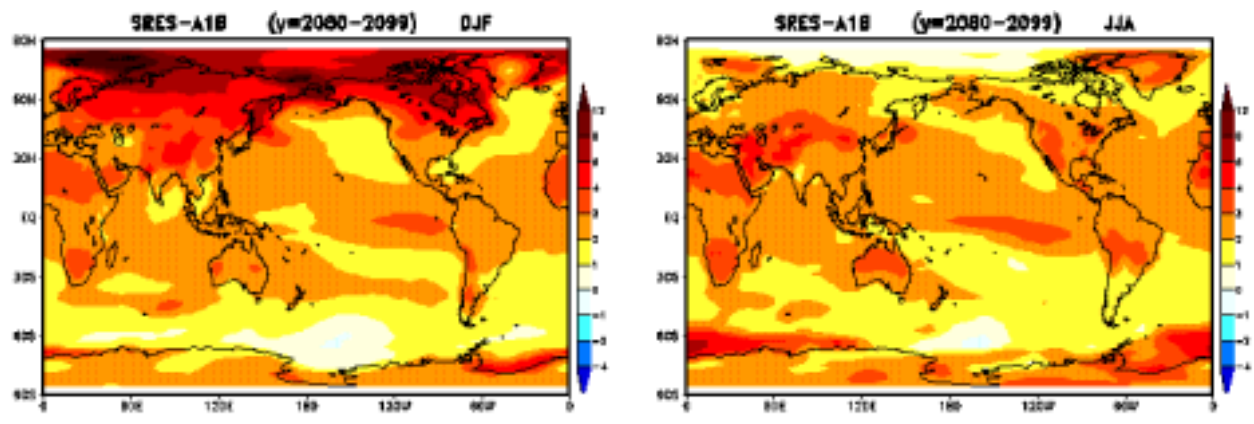


Fig. 6

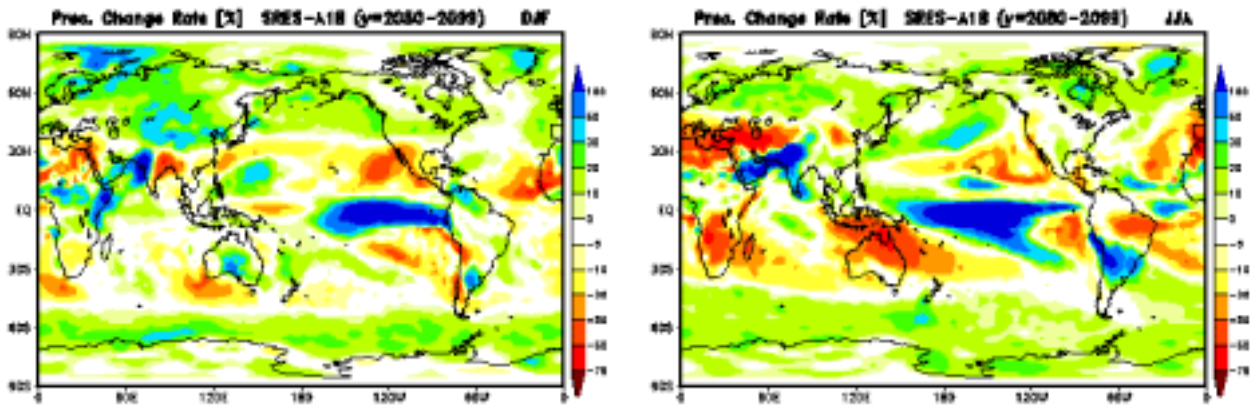


Fig. 7

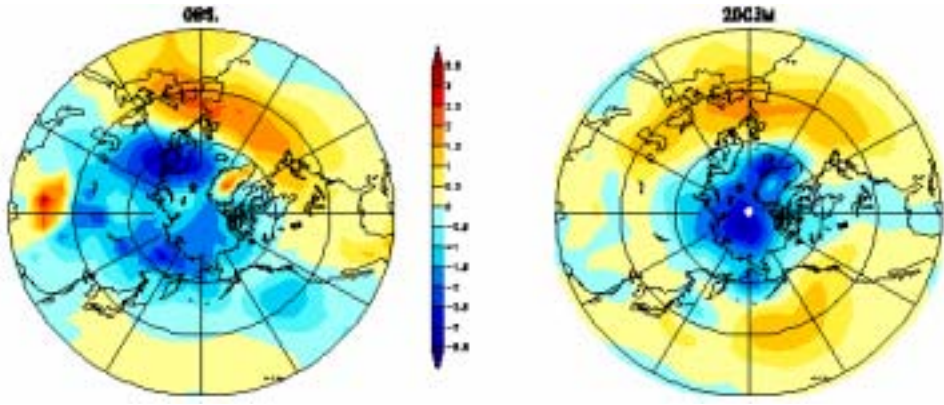


Fig. 8



Fig. 9

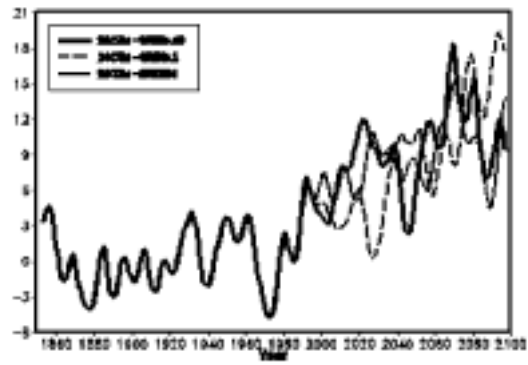


Fig. 10



Fig. 11

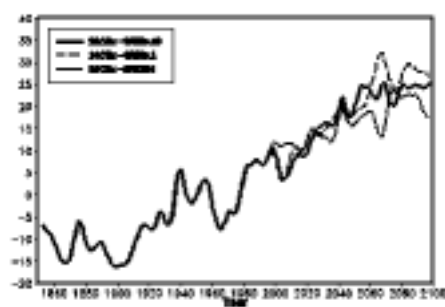


Fig. 12

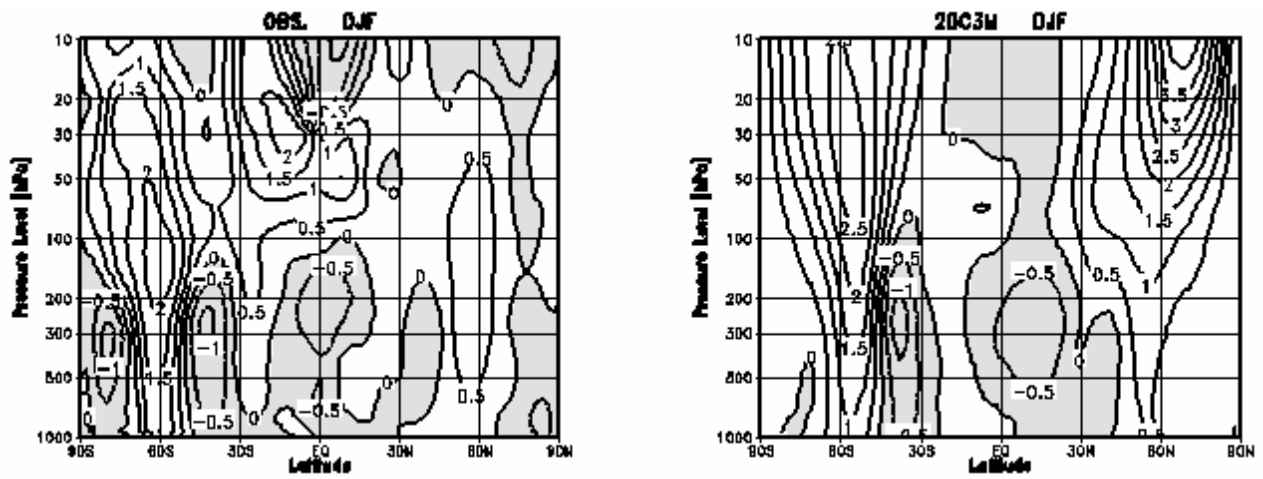


Fig. 13

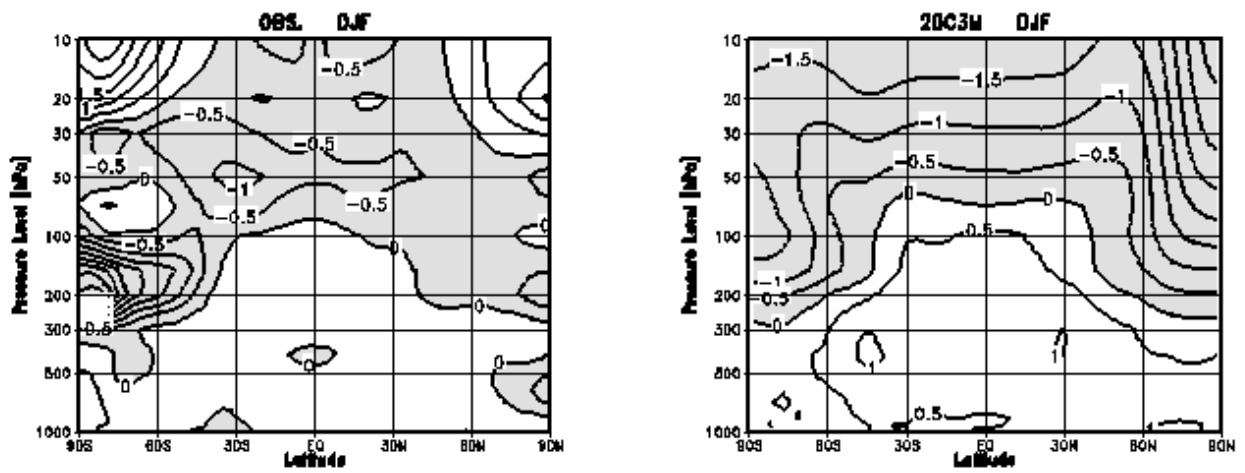


Fig. 14

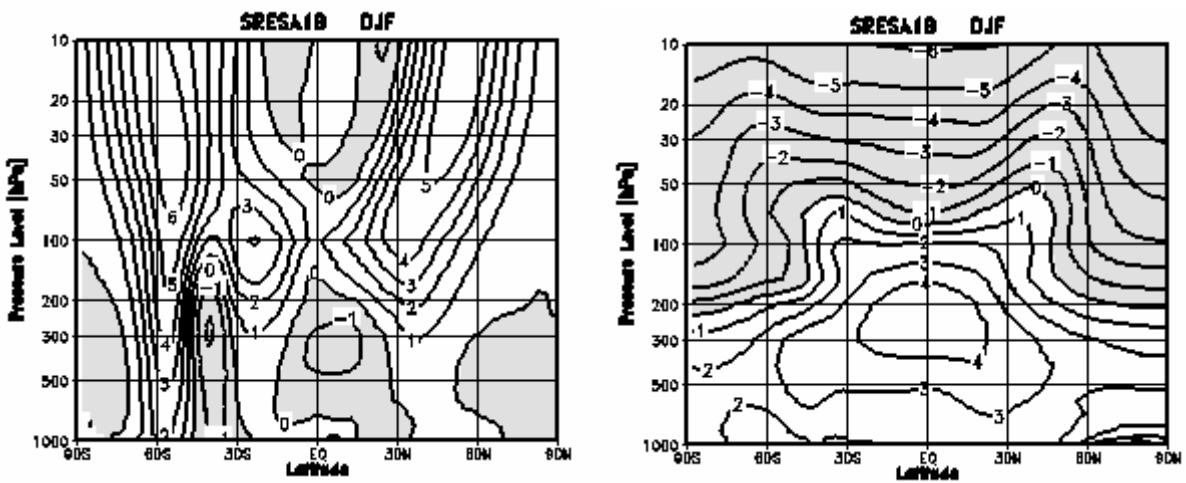


Fig. 15

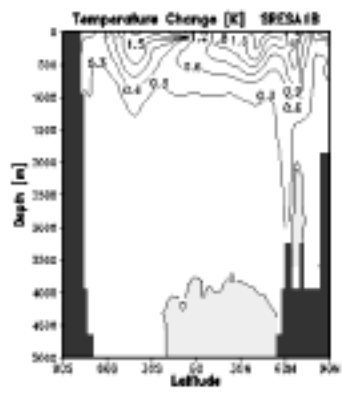


Fig. 16

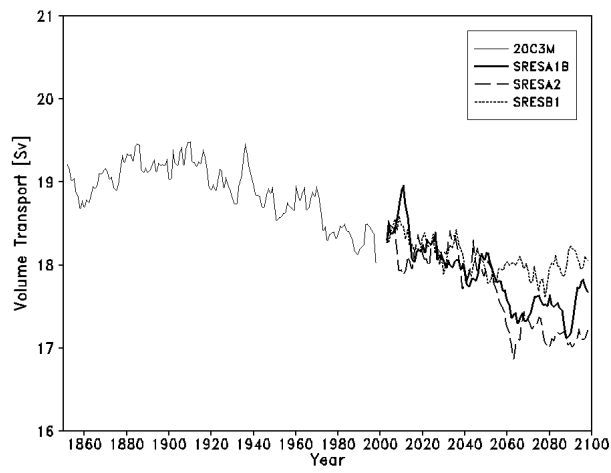


Fig. 17

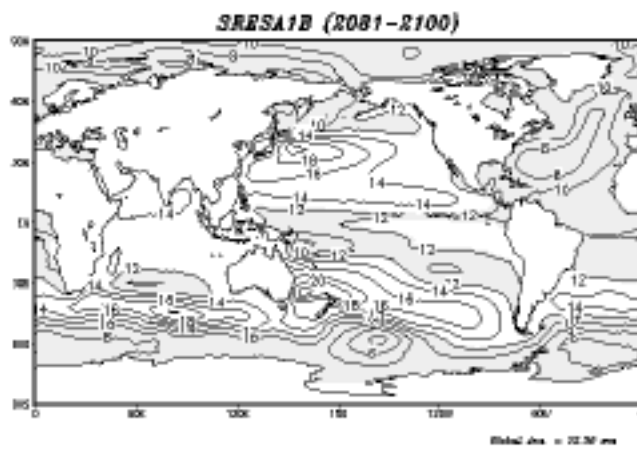


Fig. 18

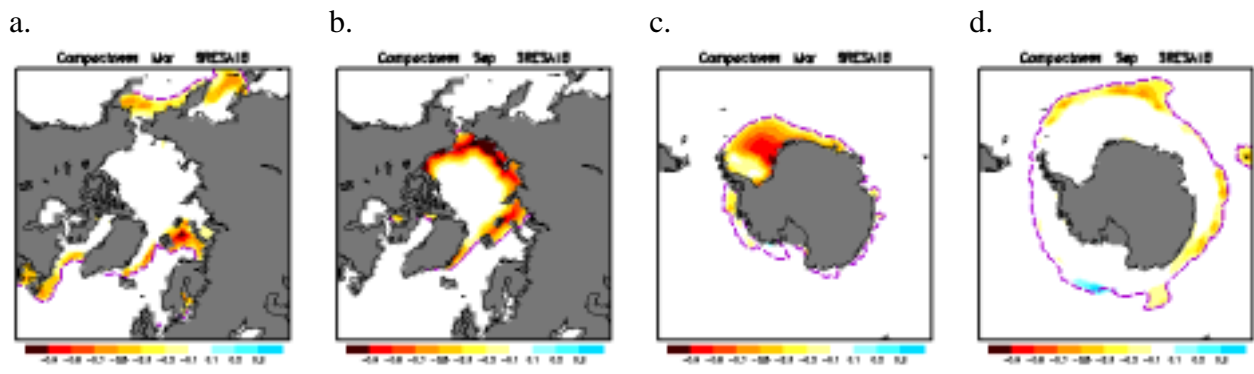


Fig. 19